Charge-exchange-dependent energy loss of H and He in freestanding monolayers of graphene and MoS_2

Anna Niggas [1,*] Lukas Fischer,[1] Silvan Kretschmer [2,†] Matthias Werl [1] Herbert Biber [1] Carsten Speckmann [3,4] Niall McEvoy,[5,6] Jani Kotakoski [3] Friedrich Aumayr [1] Arkady V. Krasheninnikov [2,7] and Richard A. Wilhelm [1,‡]

[1]*Institute of Applied Physics, TU Wien, 1040 Vienna, Austria, EU*

[2]*Institute of Ion Beam Physics and Materials Research, Helmholtz-Zentrum Dresden-Rossendorf, 01328 Dresden, Germany, EU*

[3]*Faculty of Physics, University of Vienna, 1090 Vienna, Austria, EU*

[4]*Vienna Doctoral School in Physics, University of Vienna, 1090 Vienna, Austria, EU*

[5]*School of Chemistry, Trinity College Dublin, College Green, Dublin 2, Ireland, EU*

[6]*CRANN and AMBER Research Centres, Trinity College Dublin, College Green, Dublin 2, Ireland, EU*

[7]*Department of Applied Physics, Aalto University, P.O. Box 11100, 00076 Aalto, Finland*

(Received 23 May 2023; revised 13 November 2023; accepted 22 November 2023; published 26 December 2023)

We study the energy loss of helium and hydrogen ions after transmission through monolayers of graphene and MoS_2 and compare experimental results with different computational approaches. We find a systematically higher energy loss in experiments compared to simulations by up to a factor of 2. Additionally, our results show that neutralization processes of the particles increase the kinetic energy loss, a contribution generally not included in any computational approach.

DOI: 10.1103/PhysRevA.108.062823

I. INTRODUCTION

When a charged particle penetrates matter, it interacts with the nuclei and electrons in the material via elastic and inelastic collisions. One consequence thereof is that the particle kinetic energy is reduced as it transfers energy to the target. Understanding the mechanisms underlying these processes is important, since many techniques and applications rely on ion-solid interactions such as ion-beam analysis techniques. These include low-energy ion scattering [1,2] and Rutherford backscattering [3,4], nanopatterning [5,6], and ion therapy [7,8], to name a few.

To quantify the energy transfer to the target system, one typically uses the stopping cross section $S = \frac{1}{n}\frac{dE}{ds}$ that describes the energy E transferred per length s normalized to the atomic material density n [9]. There exist many theoretical models [9–11] and simulation codes [12,13] allowing one to predict the stopping cross section for any choice of projectile-target combination; however, not all of them are well suited for every parameter regime. To benchmark these codes and refine stopping models, thin foils and ultimately two-dimensional (2D) materials have proven to be an ideal playground [14,15]: There projectiles are limited to single (or a few) collisions of well-defined collisional geometries [16].

In this study we present experimental results of charge-state-separated energy transfer of slow light ions (1–5 keV H^+ and He^+) through suspended monolayers of graphene and MoS_2. We compare the results to established binary collision approximation (BCA) codes and *ab initio* time-dependent density functional theory (TDDFT) calculations in the Ehrenfest dynamics scheme to find that simulations systematically underestimate the stopping in the 2D crystal. Specifically, we find an additional increase in the measured energy transfer due to charge-exchange processes of the ions that is not covered by the computational approaches.

Note that for the definition of the stopping cross section mentioned above, one implicitly includes all trajectories and possible scattering angles and the result is thus an average energy transfer per unit length. In ion scattering experiments, detectors are typically limited to a (small) angular range and thus only certain particle trajectories (i.e., impact parameters) contribute to the measured signal, in our case in the forward scattering direction. Our experimentally determined energy loss therefore typically underestimates the stopping cross section since large scattering angles and small impact parameters with high energy losses are not considered [9,17]. Large differences between the full stopping cross section and the partial (angle-selective) energy loss occur in particular in the single- or few-collision scattering regime, i.e., when slow ions penetrate a suspended 2D material [15], and for thicker samples in channeling geometry [18,19]. For this reason we avoid using the nomenclature of "stopping cross section," which would include all scattering angles, but adhere to discussing the "energy loss" instead.

II. METHODS

We present a joint experimental and computational effort to study the energy loss of low-energy light ions (1–5 keV H^+ and He^+) transmitted through 2D materials. As representatives we choose freestanding highly conductive single-layer

*niggas@iap.tuwien.ac.at
†s.kretschmer@hzdr.de
‡wilhelm@iap.tuwien.ac.at

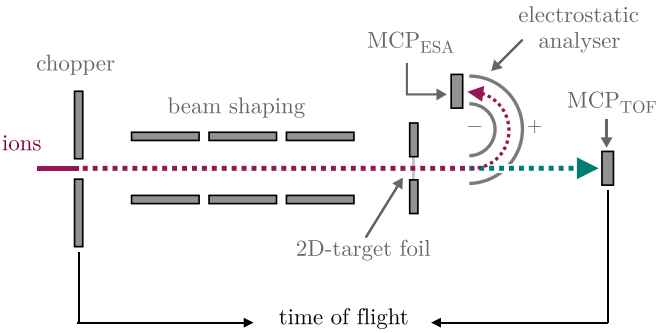

FIG. 1. Experimental setup to study the energy loss of light ions transmitted through a freestanding 2D material. An electrostatic energy analyzer (ESA) with a multichannel plate (MCP) detector is used to detect particles that are still charged after the interaction. For neutralized particles, the ion beam is chopped and the time of flight (TOF) from the chopper to an additional MCP in the forward direction is measured in order to determine the particle energy loss.

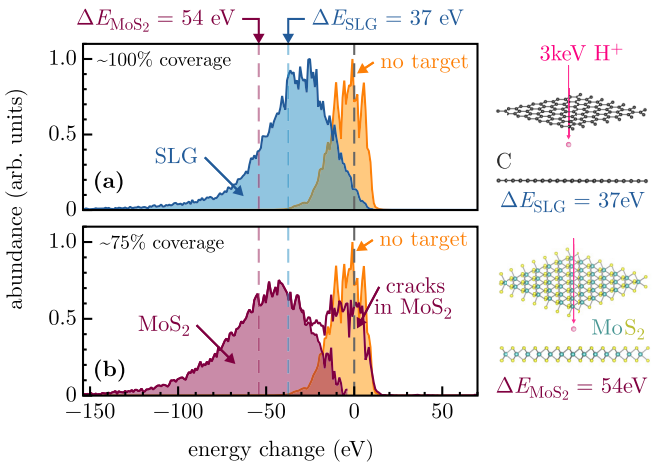

FIG. 2. Energy spectra of 3 keV H^+ transmitted through (a) graphene (SLG, blue) and (b) MoS_2 (red) are shown together with the primary beam energy profile (no target, orange). While for SLG the whole distribution shifts, which indicates a sample coverage of approximately 100%, in MoS_2 we find that 25% of the ions still overlap with the original beam profile. This can be attributed to cracks and uncovered parts of the sample. For MoS_2 we analyzed only the shifted distribution (filled with red color) to determine the energy loss given for both samples at the top of the figure. Both spectra were recorded using the electrostatic analyzer and thus present only the energy loss of the H^+ fraction that does not neutralize while transmitting the sample. A schematic representation of the experiment is shown to the right.

graphene (SLG) consisting of one layer of carbon atoms and semiconducting MoS_2. In contrast to graphene, MoS_2 has a three-layer structure with the molybdenum atoms being sandwiched in between sulfur atoms, leading to an overall thicker sample layer, i.e., 0.7 nm for MoS_2 [20] compared to 0.3 nm for SLG [21] (assuming a single layer has a thickness corresponding to the van der Waals distance in the layered bulk crystal).

A. Experimental approach

For experiments performed at TU Wien, an electron cyclotron resonance ion source is used to prepare H^+ and He^+ ions (approximately 500–800 pA) with kinetic ion energies in the range of 1–5 keV [22]. A sector magnet allows one to select the relevant ions (and charge states in case of He). By using several pairs of deflection plates and einzel lenses, the ion beam is shaped (beam diameter of approximately 0.5 mm) and steered to the target (see Fig. 1). Typically, fluences of around 10^{15} ions/cm^2 are applied. After transmission through the 2D sample, the ions enter an electrostatic energy analyzer (ESA) with a multichannel plate (MCP$_{ESA}$) at the end. By varying ESA voltages we can directly determine both the energy of the primary ions (no target) and the projectile energy after interaction with a material, respectively. This, however, applies to only charged particles. In order to be able to also consider neutralized particles, we install an electrostatic chopper in the path of the ion beam to pulse the beam and trigger a start signal for time of flight (TOF) measurements. To receive a stop signal, we place another MCP$_{TOF}$ in the forward scattering direction behind the ESA such that the particles can pass through a hole in the outer plate of the ESA. By biasing the ESA we deflect all charged particles and detect stop signals only for neutrals. Note that the chopper (i.e., a pulsed beam) is used also for ESA measurements to be able to use the same beam settings for all measurements. In both cases the measured energy loss refers to the kinetic energy. Potential energy loss is not considered in this work. A detailed description of the data acquisition tools can be found in the Appendix.

We used freestanding 2D materials placed on transmission electron microscopy (TEM) grids and Quantifoil support. Graphene samples were commercially acquired from Graphenea [23] and MoS_2 samples were produced at Trinity College Dublin [24] and transferred onto TEM grids at the University of Vienna [25]. Then the MoS_2 samples were characterized in scanning transmission electron microscopy (STEM), where an average coverage of approximately 60% was determined, ranging between 30% and 80% on different sample areas. The STEM measurements were conducted with a Nion UltraSTEM 100 using a Ronchigram charge coupled device at an electron acceleration voltage of 60 kV in bright field mode. Prior to the ion-beam spectroscopy measurements, we heated all samples to approximately 400 °C following the procedure discussed in [26]. There it was shown that this cleaning procedure leads to clean sample areas in between thick clustered contamination. Ions transmitting the latter endure much higher energy loss and can therefore be neglected in the analysis of required data to focus solely on the atomically thin material.

Figure 2 shows a schematic representation of the experiment (right) as well as exemplary ESA spectra of 3 keV H^+ transmitted through SLG [blue, Fig. 2(a)] and MoS_2 [red, Fig. 2(b)]. Orange distributions represent the primary beam (without interaction with a sample). A shift in energy is observed for both SLG and MoS_2, but while the whole distribution shifts for graphene, for MoS_2 there is a fraction of ions that is still detected with the primary ion energy (red curve). This fraction amounts to approximately 25%, corresponding well to the uncovered area as found by STEM in the

precharacterization. We therefore subtract a scaled primary beam from the spectrum in order to achieve the ion energy distribution after transmission through MoS_2 (red colored area). The energy loss is then determined by taking the means of the distributions and comparing them to the mean of the primary beam distribution. This results in $\Delta E_{\mathrm{SLG}} = 37$ eV and $\Delta E_{\mathrm{MoS_2}} = 54$ eV, as indicated at the top of the figure.

B. Computational approach

In order to model both energy and charge transfer during the single-charge ion transmission, we performed Ehrenfest dynamics simulations based on TDDFT for the electronic subsystem as implemented in the GPAW package [27–29]. The nuclei were treated as classical particles. For that, we relaxed the 2D material supercells consisting of about 100 atoms with a grid spacing of 0.2 Å such that all forces on atoms in the Γ-point calculations are smaller than 0.01 eV/Å. We then prepared the initial charge state of the ion placed 5 Åaway from the 2D sheet using constrained density functional theory on a Γ-point k-point mesh [30]. Consequently, Ehrenfest dynamics was started with the same k-point mesh and the previously determined electron density and ion velocity being set according to the initial kinetic energy of the projectile. Results for the energy loss compare well with previous Ehrenfest dynamics simulation for proton irradiated graphene [31–36].

We further benchmark our *ab initio* results against established codes based on the binary collision approximation: SRIM [12] and SDTRIMSP [13] (using the graphical user interface published in [37]). Both use amorphous material layers as targets, where we set up our systems with densities of 2.266 g cm^{-2} for graphene and 5.06 g cm^{-2} for MoS_2. As for the thickness of the material layers, we used the appropriate interlayer spacing of 3.34 Å (graphene) and 6.15 Å (MoS_2). In SRIM, we selected the type "detailed calculation with full damage cascades." In SDTRIMSP, the universal potential is applied and the Lindhard-Scharff model ("inel0=1") was chosen to estimate the inelastic stopping.

III. RESULTS

GPAW computations were performed for transmission of single-charge hydrogen and helium ions through monolayers of graphene and MoS_2. A number of different ion impact parameters were calculated for different kinetic energies and each projectile-sample pair. The energy loss was then averaged over all impact parameters per kinetic energy. In Fig. 3(a) our results are shown in dependence on the projectile velocity, where hydrogen is given as circles and helium as triangles. Single-layer graphene is colored blue and MoS_2 red. As dotted lines we added the energy loss obtained from Lindhard-Scharff theory for electronic stopping

$$\left.\frac{\mathrm{d}E}{\mathrm{d}x}\right|_e = S_e = 8\pi a_0 \rho \frac{e^2}{4\pi\epsilon_0}\frac{Z_i Z_t}{Z_s}\frac{v_{\mathrm{ion}}}{v_0}\xi_e, \tag{1}$$

where $a_0 = 0.529$ Å is the Bohr radius, $v_0 = 2.18$ nm/fs is the first Bohr velocity, ρ is the target material atom (number) density, Z_i and Z_t are the atomic numbers of the ion and target, respectively, $Z_s = (Z_i^{2/3} + Z_t^{2/3})^{3/2}$ is a screening parameter, and $\xi_e \sim Z_i^{1/6}$ in between 1 and approximately 2 accounts

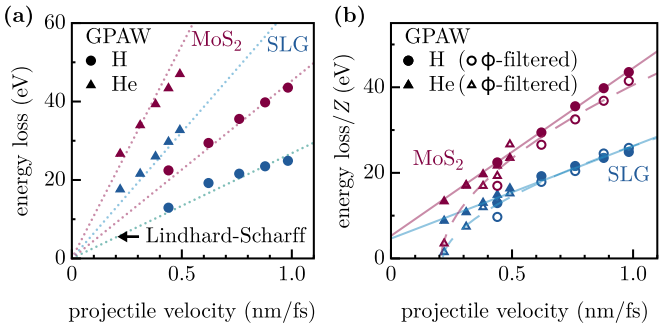

FIG. 3. Simulated kinetic energy loss of protons (circles) and helium ions (triangles) for transmission through monolayers of graphene (SLG, blue) and MoS_2 (red) as modeled by Ehrenfest dynamics with the GPAW package. In (a) the energy loss is compared to Lindhard-Scharff theory, where in both cases a linear dependence is seen. For (b) the energy loss of helium is scaled with $1/Z$, which makes data points for H and He become collinear. Closed symbols show the average energy loss for all calculated impact parameters whereas open symbols take into account only ions scattered into a polar angle of $\phi = 2^\circ$. Fits were added for both data sets to guide the eye.

for variations [38]. Here we used ξ_e as a fitting parameter and obtained $\xi_{\mathrm{H,SLG}} = 1.2$, $\xi_{\mathrm{He,SLG}} = 1.44$, $\xi_{\mathrm{H,MoS_2}} = 1.8$, and $\xi_{\mathrm{He,MoS_2}} = 2.16$.

By scaling the energy loss with the projectile atomic number $1/Z$ as motivated in (1), a universal trend can be found, as depicted in Fig. 3(b). Note that there is also a Z dependence in the denominator, which is however overall dominated by the material target atomic number when using light ions.

Depending on the ion-material combination, we find different scattering angles of incident particles in GPAW calculations, e.g., hydrogen on graphene scatters into much smaller cones compared to helium on MoS_2 (see Fig. 4). The energy loss for hydrogen [Figs. 4(a) and 4(b)] and helium [Figs. 4(c) and 4(d)] after transmission through monolayers of graphene [Figs. 4(a) and 4(c)] and MoS_2 [Figs. 4(b) and 4(d)] is given in the form of a kinetic energy vs scattering angle ϕ heat map. Taking the average of all possible scattering angles is however not comparable to the experiment, where the detector only has an acceptance angle of approximately 1°. For this reason we filtered GPAW data according to the particle scattering angle ϕ to better represent the experiment (the limit is indicated as a pink dashed line in Fig. 4). This in general underestimates the stopping cross section with increasing significance for decreasing projectile velocities. Note that $\phi \leqslant 2^\circ$ was used for all simulations as a filtering condition, in order to retain reasonable statistics. Filtered data points are also plotted in Fig. 3 as open symbols.

A comparison of the ϕ-filtered GPAW results with experiments is shown in Fig. 5. The GPAW data are given as a solid line [i.e., the fit shown in Fig. 3 (a)] and experimental results are plotted as circles. There we distinguish between particles that are still charged ($q_{\mathrm{out}} = 1$) and particles that are neutral ($q_{\mathrm{out}} = 0$) after transmission through the atomically thin material. Note that we did not observe a charging up, i.e., for He projectiles we only discuss singly charged states. For $q_{\mathrm{out}} = 1$ we used the electrostatic analyzer, while for $q_{\mathrm{out}} = 0$

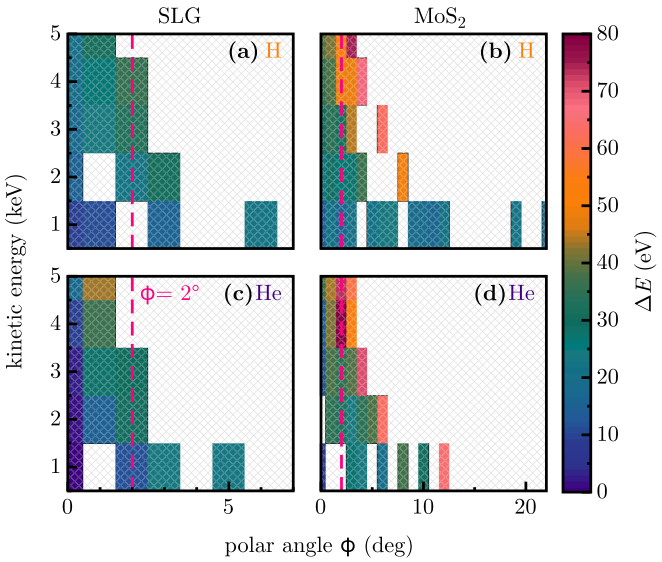

FIG. 4. Energy loss ΔE for 1–5 keV (a) and (b) H^+ and (c) and (d) He^+ ions transmitted through (a) and (c) monolayers of graphene and (b) and (d) MoS_2. For every kinetic energy, modeled trajectories were binned regarding their polar scattering angle ϕ, where larger ϕ correspond to higher energy loss and charge exchange. Due to high computational effort, data could not be obtained for all bins.

we relied on time of flight measurements. Additional computational data are added from BCA codes SRIM and SDTRIMSP. For both codes we saved listmode files for the results in order to apply the same $\phi \leqslant 2^\circ$ condition we also used for GPAW. For SDTRIMSP, we used the additional possibility to limit

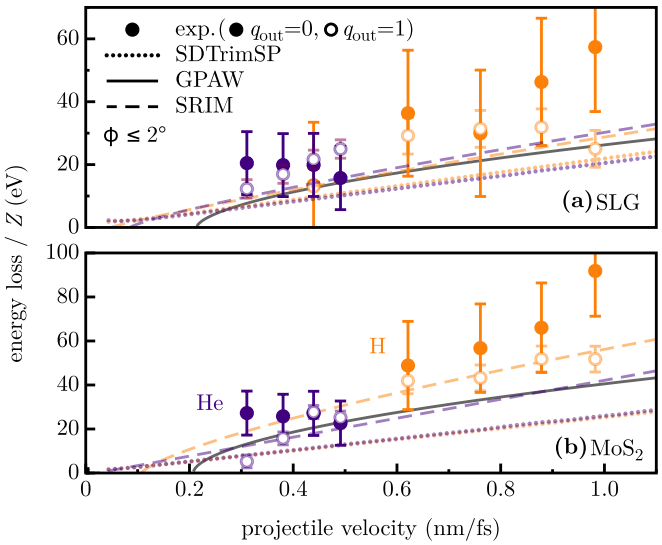

FIG. 5. Comparison of experimental data (circles) to numerical determination of the kinetic energy loss of H^+ (orange) and He^+ (violet) in (a) SLG and (b) MoS_2. For experiments, results are given for exit charge states $q_{out} = 0$ (closed circles) and $q_{out} = 1$ (open circles). For GPAW the fit introduced in Fig. 3(b) is added as a solid line. The SRIM and SDTRIMSP results are plotted as dashed and dotted lines, respectively. All computational results are filtered for polar angles $\phi \leqslant 2^\circ$. An explanation of how error bars were determined can be found in the Appendix.

the number of collisions to a maximum of 2. That way we suppress particles that are scattered in the chosen scattering angle due to multiple collisions, something unlikely for a monolayer material but may occur in the amorphous target approximations in our BCA codes. For all presented helium results, we applied a scaling of $1/Z$.

IV. DISCUSSION

For all approaches used in this study of the energy loss of charged particles transmitting through monolayers of graphene and MoS_2, we find a linear increase in energy loss with increasing projectile velocity. This agrees well with Lindhard-Scharff theory for electronic stopping [11] predicting an energy loss approximately equal to v as shown in Eq. (1). Also a scaling with the projectile atomic number Z according to Lindhard-Scharff theory can be observed. Note that only at small projectile velocities is a linear Z dependence expected, whereas at higher velocities a scaling with Z^2 would be applicable [9]. In terms of absolute values, we find that our energy loss results are well within the same order of magnitude, but our simulations are about 60% smaller than experimental values. Experimental values show good agreement with literature data using few-layer graphene samples [39,40], where, e.g., for 2 keV H^+ projectiles, energy losses of 10–15 eV/Åwere found. Considering the theoretical thickness of 3.34 Å, this yields energy losses for single-layer graphene, which are well comparable with our measurements (approximately 10 eV/Å).

One of the main advantages of our experiments with ultrathin materials is the possibility to study the energy loss in dependence on charge-exchange processes in the material. Here, in general, we find a higher energy loss in experiments than for all conducted computations, with small deviations for particles that are still charged ($q_{out} = 1$) and a difference of a factor of up to 2 for neutralized particles ($q_{out} = 0$). While literature data on charge-state-dependent energy loss of slow light ions are scarce, we find good agreement with recent results for slow highly charged ions in 2D materials [41] and 1-nm-thick carbon nanomembranes [42] as well as for medium-energy ions in approximately 25-nm amorphous carbon foils [14], where also an increasing energy loss for smaller exit charge states was found. In contrast to results in Refs. [14,41,42] where all data points were acquired using the same detector, here we applied two different approaches to achieve data for neutral and charged particles. To rule out an influence of the two different methods used to acquire data for $q_{out} = 0$ and $q_{out} = 1$, we performed a control measurement with our time of flight setup where we can choose to detect only neutrals (ESA on) or both charged and neutral particles (ESA off). An exemplary spectrum is shown in Fig. 6 in the Appendix. There we also find a higher energy loss for the neutralized particles.

All simulation data (lines in Fig. 5) are systematically below our experimental data (points). This could, on the one hand, be explained by contamination on the samples. However, as discussed in Sec. II, we applied an established procedure to prepare clean samples and are thus confident that we studied indeed clean freestanding 2D materials. Nevertheless, as it was not possible to check cleanliness *in situ*, we

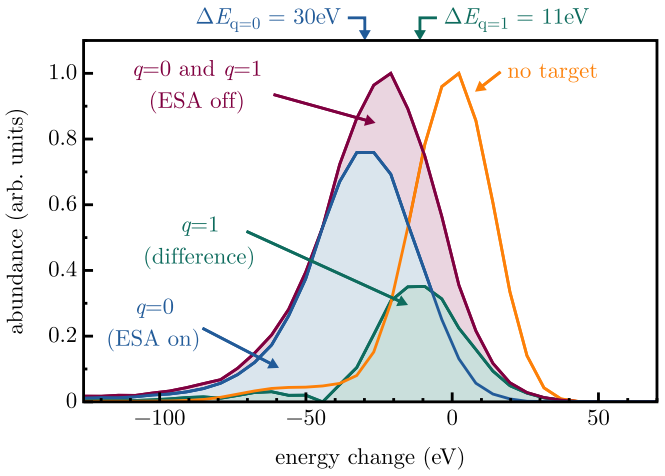

FIG. 6. Time of flight spectrum (translated to energy) of 3 keV H^+ ions transmitted through a monolayer of graphene.

cannot completely rule out any influence from contamination on the sample. For comparison, we performed another SRIM simulation using a graphene layer with a second monolayer of carbon on top mimicking contaminants. There we found an increased stopping by a factor of 2. This is an even larger value than our result for neutralized particles ($q_{\text{out}} = 0$); hence we can estimate that our sample has at maximum one atomic layer of contamination. However, for this monolayer we can expect, according to [26], that during sample heating the contamination forms thicker clusters leaving clean areas in between. Since the energy loss of particles in the latter would separate significantly from the contaminated areas in our experiments, we suggest that our results indeed represent a clean 2D material.

To explore other explanations for the systematic difference between experimental and computational data, let us review the main features of the simulation codes applied. As BCA codes, SRIM and SDTRIMSP model a neutral particle trajectory inside an amorphous material by generating subsequent two-particle nuclear collisions and solving the classical scattering integral using the universal potential [12,13]. The distance between two collisions is inversely dependent on the material density. The electronic energy loss is accounted for according to the distance traveled in the material. Here SDTRIMSP uses the Lindhard-Scharff [11] stopping model. Ziegler *et al.* however showed in Ref. [9] that while Lindhard stopping matches experimental data well for high energies, it typically underestimates the stopping for low energies (less than 1 MeV/amu). They therefore determined a fractional effective charge $\gamma^2 = \frac{S_{\text{expt}}}{S_{\text{theory}}}$ from experimental S_{expt} and theoretical S_{theory} stopping values in order to correct for that deviation at small energies. This artificial correction of the electronic stopping model used in SRIM in the energy range essential for our experiments can explain the overall better agreement of SRIM data with our experiments. In particular, we observe that $q_{\text{out}} = 1$ data points from our experiments are very close to computational SRIM results. We assume that the experiments, on which SRIM's γ factor is based, were mainly conducted studying particles without any charge exchange, which would make this behavior reasonable. However, we cannot unambiguously verify this statement because of missing references in [9].

Unlike this indirect charge-state inclusion in SRIM, the projectile charge can be assessed in GPAW directly. In TDDFT electrons are generally treated in the form of an electron density and solving the Kohn-Sham equations of this system for every time step makes it an *ab initio* calculation with high computational effort. It further allows the declaration of a sample unit cell providing a more realistic (i.e., crystalline) environment for the simulation of particle transmission through a monolayer of material. For neutral projectiles, GPAW was successfully applied to study the energy loss during transmission of a monolayer of graphene [43]. To model a charged particle, the electron density around the projectile needs to be adapted. For hydrogen this leaves a bare proton and for helium a nonempty shell. The latter forms a much more complex system, which explains scarce literature on this topic [31,44].

By integrating the electron density around the projectile after transmission, we get access to the charge state of the projectile. This charge state decreases with kinetic energy and lies between $q_{\text{out}} = 0.40$ (5 keV) and $q_{\text{out}} = 0.24$ (1 keV) for H^+ transmission through graphene. In MoS_2 we observe the same trend with slightly smaller charges of $q_{\text{out}} = 0.25$ (5 keV) and $q_{\text{out}} = 0.08$ (1 keV). This agrees well with recent experiments [41,45,46]. Using the TOF spectrum in Fig. 6 in the Appendix, we can also estimate a mean charge of $q_{\text{out}} = 0.37$ for 3 keV H^+ transmitted through graphene, which is slightly higher than the respective GPAW value of $q_{\text{out}} = 0.27$. The difference might be explained by our experiment underestimating the number of neutral particles due to their typically larger scattering angles that are not covered by our detector.

We would thus expect the resulting energy loss from GPAW to lie in between experimental data for $q_{\text{out}} = 0$ and 1. This is however not the case. We find good agreement of GPAW with SRIM and TDDFT data presented in [31,43,44] instead. One possible explanation for the discrepancy of GPAW with our experiment could be the lack of electronic transitions in BCA codes and GPAW that are however contributing significantly to the energy loss in experiment, especially for neutralizing particles. Similar experiments with highly charged ions showing a charge-exchange-dependent increase in the energy loss [42], as well as studies discussing that resonant electron transfer alone does not influence the energy loss of multiply charged ions in thin materials [47], fit very well with this picture. In Ref. [48] we discussed that any charge-exchange process leads to an inelastic deformation of the scattering potential and thus to an additional energy loss channel.

V. CONCLUSION

We discussed that experimental energy loss data of light ions transmitted through atomically thin materials are systematically higher than simulations by a factor of about 60%. We applied both binary collision approximation codes (SRIM and SDTRIMSP) and *ab initio* time-dependent density functional theory calculations (GPAW). While we could correctly reproduce the trends in the stopping in dependence on the velocity, we observed an absolute offset for all used simulation codes. One explanation for this could be contaminated samples;

however, due to the cleaning scheme applied, we are confident that we studied mainly clean sample areas.

One major difference between simulations and experiments is that in the latter one can directly access the charge state of the projectiles after interaction with the material. Thereby we showed that charge-exchange processes generally increase the kinetic energy loss compared to particles that leave the material with their incident charge state. This demonstrates that studying especially this regime is important and further experiments are necessary to understand the behavior in order to refine models and to be able to reliably simulate the energy loss of charged particles in matter.

ACKNOWLEDGMENTS

The authors would like to acknowledge funding from the Austrian Science Fund (FWF) via Projects 10.55776/Y1174, 10.55776/I4914, 10.55776/P36264, and 10.55776/I4101 and through doctoral college Advanced Functional Materials–Hierarchical Design of Hybrid Systems. A.N. and R.A.W. acknowledge funding from TU Wien's Innovative Project Fund. A.V.K. is grateful to the German Research Foundation (DFG) for support through Project No. KR 4866/9-1 and the collaborative research center Chemistry of Synthetic 2D Materials through Grant No. CRC-1415-417590517. Generous CPU time grants from the Technical University of Dresden computing cluster (TAURUS) and Gauss Centre for Supercomputing e.V., Supercomputer HAWK at Hochstleistungsrechenzentrum Stuttgart, are greatly appreciated.

APPENDIX

Additional comments on the methods, data analysis, and results can be found in the following.

Electronics for data acquisition. A function generator triggers the Spezialpuls 003 (GBS Spezialelektronik GmbH), which delivers a bipolar pair of voltages for the chopper deflection plates. The chopper frequency and pulse length are selected according to the ion species in order to optimize the count rate by still allowing enough time for the ions to pass the detector while the voltage is turned off. Another branch of the function generator is fed to a time-to-amplitude converter (TAC). The second time stamp for the TAC is delivered by the amplified signal from the MCP_{TOF}. Times of flight are therewith translated into pulse heights, which are further analyzed with a multichannel analyzer. For the ESA, data acquisition is performed using solely an amplifier including a TTL signal generator for the MCP_{ESA} signal and a counter.

Time of flight measurements. An example TOF measurement (where the TOF axis is already converted to energy) can be found in Fig. 6 for 3 keV H^+ transmitted through a monolayer of graphene. The primary beam is depicted using an orange line. We can choose either to detect all particles ($q_{out} = 0$ and 1, red) or to deflect charged particles using the ESA voltages to detect only the neutrals (blue). The difference of both spectra then gives us the distribution of charged particles (green). The overall trend seen also in Fig. 5 that neutralized particles lose more energy in the material is visible also in this exemplary spectrum.

Uncertainties of measurements. A number of uncertainties were taken into account to determine error bars for the experimental data presented in Fig. 5. First we calculated the statistical error from the number of data points in our measured distributions (approximately 1 eV). To assess the stability of the measurement method itself, we controlled measurements over the course of two days, repeating the same measurement about ten times for both ESA (approximately 1 eV) and TOF (approximately 1–5 eV) measurements. For the TOF we also included sudden shifts of the beam due to electronic reasons on the order of approximately 20 eV. For the ESA an additional source of error is the incident angle of the ion beam. To account for that we varied the ESA voltage by ± 1.25 V (approximately 6 eV) to see how it influences the calculated ion energy.

[1] H. Brongersma, M. Draxler, M. Deridder, and P. Bauer, Surface composition analysis by low-energy ion scattering, Surf. Sci. Rep. **62**, 63 (2007).

[2] C. V. Cushman, P. Brüner, J. Zakel, G. H. Major, B. M. Lunt, N. J. Smith, T. Grehl, and M. R. Linford, Low energy ion scattering (LEIS). A practical introduction to its theory, instrumentation, and applications, Anal. Methods **8**, 3419 (2016).

[3] D. Schulz-Ertner and H. Tsujii, Particle radiation therapy using proton and heavier ion beams, J. Clin. Oncol. **25**, 953 (2007).

[4] M. V. Moro, P. Bauer, and D. Primetzhofer, Experimental electronic stopping cross section of transition metals for light ions: Systematics around the stopping maximum, Phys. Rev. A **102**, 022808 (2020).

[5] J. Gierak, Focused ion beam nano-patterning from traditional applications to single ion implantation perspectives, Nanofabrication **1**, 35 (2014).

[6] T. T. Tran, H. Bruce, N. H. Pham, and D. Primetzhofer, A contactless single-step process for simultaneous nanoscale patterning and cleaning of large-area graphene, 2D Mater. **10**, 025017 (2023).

[7] W. T. Chu, B. A. Ludewigt, and T. R. Renner, Instrumentation for treatment of cancer using proton and light-ion beams, Rev. Sci. Instrum. **64**, 2055 (1993).

[8] M. Durante and H. Paganetti, Nuclear physics in particle therapy: A review, Rep. Prog. Phys. **79**, 096702 (2016).

[9] J. Ziegler, J. P. Biersack, and U. Littmark, *The Stopping and Ranges of Ions in Solids* (Pergamon, Oxford, 1985), Vol. 1.

[10] P. Sigmund, Stopping of slow ions, Bull. Russ. Acad. Sci.: Phys. **72**, 569 (2008).

[11] J. Lindhard and M. Scharff, Energy dissipation by ions in the kev region, Phys. Rev. **124**, 128 (1961).

[12] J. Ziegler, M. Ziegler, and J. Biersack, SRIM—The stopping and range of ions in matter (2010), Nucl. Instrum. Methods Phys. Res. Sect. B **268**, 1818 (2010).

[13] A. Mutzke, R. Schneider, W. Eckstein, R. Dohmen, K. Schmid, U. von Toussaint, and G. Badelow, SDTrimSP version 6.00, IPP Report No. 2019-02, 2019 (unpublished), available

at https://pure.mpg.de/rest/items/item_3026474_2/component/file_3026477/content.

[14] R. Holeňák, S. Lohmann, F. Sekula, and D. Primetzhofer, Simultaneous assessment of energy, charge state and angular distribution for medium energy ions interacting with ultra-thin self-supporting targets: A time-of-flight approach, Vacuum **185**, 109988 (2021).

[15] S. Creutzburg, A. Niggas, D. Weichselbaum, P. L. Grande, F. Aumayr, and R. A. Wilhelm, Angle-dependent charge exchange and energy loss of slow highly charged ions in freestanding graphene, Phys. Rev. A **104**, 042806 (2021).

[16] M. Ćosić, S. Petrović, and N. Nešković, The forward rainbow scattering of low energy protons by a graphene sheet, Nucl. Instrum. Methods Phys. Res. Sect. B **422**, 54 (2018).

[17] P. L. Grande and G. Schiwietz, Impact-parameter dependence of the electronic energy loss of fast ions, Phys. Rev. A **58**, 3796 (1998).

[18] S. Lohmann and D. Primetzhofer, Disparate energy scaling of trajectory-dependent electronic excitations for slow protons and He ions, Phys. Rev. Lett. **124**, 096601 (2020).

[19] S. Lohmann, R. Holeňák, P. L. Grande, and D. Primetzhofer, Trajectory dependence of electronic energy-loss straggling at keV ion energies, Phys. Rev. B **107**, 085110 (2023).

[20] A. Splendiani, L. Sun, Y. Zhang, T. Li, J. Kim, C.-Y. Chim, G. Galli, and F. Wang, Emerging photoluminescence in monolayer MoS_2, Nano Lett. **10**, 1271 (2010).

[21] Z. H. Ni, H. M. Wang, J. Kasim, H. M. Fan, T. Yu, Y. H. Wu, Y. P. Feng, and Z. X. Shen, Graphene thickness determination using reflection and contrast spectroscopy, Nano Lett. **7**, 2758 (2007).

[22] E. Galutschek, R. Trassl, E. Salzborn, F. Aumayr, and H. Winter, Compact 14.5 GHz all-permanent magnet ECRIS for experiments with slow multicharged ions, J. Phys.: Conf. Ser. **58**, 395 (2007).

[23] Graphene on TEM grids, https://www.graphenea.com (Granphenea, Inc., Cambridge, 2019).

[24] M. O'Brien, N. McEvoy, T. Hallam, H.-Y. Kim, N. C. Berner, D. Hanlon, K. Lee, J. N. Coleman, and G. S. Duesberg, Transition metal dichalcogenide growth via close proximity precursor supply, Sci. Rep. **4**, 7374 (2015).

[25] J. C. Meyer, C. O. Girit, M. F. Crommie, and A. Zettl, Hydrocarbon lithography on graphene membranes, Appl. Phys. Lett. **92**, 123110 (2008).

[26] A. Niggas, J. Schwestka, S. Creutzburg, T. Gupta, D. Eder, B. C. Bayer, F. Aumayr, and R. A. Wilhelm, The role of contaminations in ion beam spectroscopy with freestanding 2D materials: A study on thermal treatment, J. Chem. Phys. **153**, 014702 (2020).

[27] J. J. Mortensen, L. B. Hansen, and K. W. Jacobsen, Real-space grid implementation of the projector augmented wave method, Phys. Rev. B **71**, 035109 (2005).

[28] J. Enkovaara, C. Rostgaard, J. Mortensen, J. Chen, M. Dulak, L. Ferrighi, J. Gavnholt, C. Glinsvad, V. Haikola, H. Hansen, H. Kristoffersen, M. Kuisma, A. Larsen, L. Lehtovaara, M. Ljungberg, O. Lopez-Acevedo, P. Moses, J. Ojanen, T. Olsen, V. Petzold *et al.*, Electronic structure calculations with GPAW: A real-space implementation of the projector augmented-wave method, J. Phys.: Condens. Matter **22**, 253202 (2010).

[29] M. Walter, H. Häkkinen, L. Lehtovaara, M. Puska, J. Enkovaara, C. Rostgaard, and J. J. Mortensen, Time-dependent density-functional theory in the projector augmented-wave method, J. Chem. Phys. **128**, 244101 (2008).

[30] M. Melander, E. O. Jonsson, J. J. Mortensen, T. Vegge, and J. M. Garcia Lastra, Implementation of constrained DFT for computing charge transfer rates within the projector augmented wave method, J. Chem. Theory Comput. **12**, 5367 (2016).

[31] A. Kononov and A. Schleife, Anomalous stopping and charge transfer in proton-irradiated graphene, Nano Lett. **21**, 4816 (2021).

[32] A. Ojanperä, A. V. Krasheninnikov, and M. Puska, Electronic stopping power from first-principles calculations with account for core electron excitations and projectile ionization, Phys. Rev. B **89**, 035120 (2014).

[33] J. Halliday and E. Artacho, Anisotropy of electronic stopping power in graphite, Phys. Rev. B **100**, 104112 (2019).

[34] S. Zhao, W. Kang, J. Xue, X. Zhang, and P. Zhang, Comparison of electronic energy loss in graphene and BN sheet by means of time-dependent density functional theory, J. Phys.: Condens. Matter **27**, 025401 (2015).

[35] S. Bubin, B. Wang, S. Pantelides, and K. Varga, Simulation of high-energy ion collisions with graphene fragments, Phys. Rev. B **85**, 235435 (2012).

[36] A. Schleife, Y. Kanai, and A. A. Correa, Accurate atomistic first-principles calculations of electronic stopping, Phys. Rev. B **91**, 014306 (2015).

[37] P. Szabo, D. Weichselbaum, H. Biber, C. Cupak, A. Mutzke, R. Wilhelm, and F. Aumayr, Graphical user interface for SDTrimSP to simulate sputtering, ion implantation and the dynamic effects of ion irradiation, Nucl. Instrum. Methods Phys. Res. Sect. B **522**, 47 (2022).

[38] A. Guesmia, H. Ammi, S. Mammeri, A. Dib, C. Pineda-Vargas, M. Msimanga, and M. Hedibel, Semi empirical formula for electronic stopping power determination of ^{24}Mg, ^{27}Al and ^{28}Si ions crossing Formvar foil in the ion energy domain of LSS theory, Radiat. Phys. Chem. **96**, 205 (2014).

[39] F. Allegrini, P. Bedworth, R. W. Ebert, S. A. Fuselier, G. Nicolaou, and S. Sinton, Energy loss and straggling of 1–50 keV H, He, C, N, and O ions passing through few layer graphene, Nucl. Instrum. Methods Phys. Res. Sect. B **358**, 223 (2015).

[40] J. Uribe, M. Mery, B. Fierro, R. Cardoso-Gil, I. Abril, R. Garcia-Molina, J. Valdés, and V. Esaulov, Proton energy loss in multilayer graphene and carbon nanotubes, Radiat. Eff. Defects Solids **173**, 93 (2018).

[41] S. Creutzburg, J. Schwestka, A. Niggas, H. Inani, M. Tripathi, A. George, R. Heller, R. Kozubek, L. Madauß, N. McEvoy, S. Facsko, J. Kotakoski, M. Schleberger, A. Turchanin, P. L. Grande, F. Aumayr, and R. A. Wilhelm, Vanishing influence of the band gap on the charge exchange of slow highly charged ions in freestanding single-layer MoS_2, Phys. Rev. B **102**, 045408 (2020).

[42] R. A. Wilhelm, E. Gruber, R. Ritter, R. Heller, S. Facsko, and F. Aumayr, Charge exchange and energy loss of slow highly charged ions in 1 nm thick carbon nanomembranes, Phys. Rev. Lett. **112**, 153201 (2014).

[43] C. Brand, M. Debiossac, T. Susi, F. Aguillon, J. Kotakoski, P. Roncin, and M. Arndt, Coherent diffraction of hydrogen through the 246 pm lattice of graphene, New J. Phys. **21**, 033004 (2019).

[44] H. Vázquez, A. Kononov, A. Kyritsakis, N. Medvedev, A. Schleife, and F. Djurabekova, Electron cascades and secondary electron emission in graphene under energetic ion irradiation, Phys. Rev. B **103**, 224306 (2021).

[45] A. Niggas, S. Creutzburg, J. Schwestka, B. Wöckinger, T. Gupta, P. L. Grande, D. Eder, J. P. Marques, B. C. Bayer, F. Aumayr, R. Bennett, and R. A. Wilhelm, Peeling graphite layer by layer reveals the charge exchange dynamics of ions inside a solid, Commun. Phys. **4**, 180 (2021).

[46] A. Niggas, J. Schwestka, K. Balzer, D. Weichselbaum, N. Schlünzen, R. Heller, S. Creutzburg, H. Inani, M. Tripathi, C. Speckmann, N. McEvoy, T. Susi, J. Kotakoski, Z. Gan, A. George, A. Turchanin, M. Bonitz, F. Aumayr, and R. A. Wilhelm, Ion-induced surface charge dynamics in freestanding monolayers of graphene and probed by the emission of electrons, Phys. Rev. Lett. **129**, 086802 (2022).

[47] J. I. Juaristi, A. Arnau, P. M. Echenique, C. Auth, and H. Winter, Charge state dependence of the energy loss of slow ions in metals, Phys. Rev. Lett. **82**, 1048 (1999).

[48] R. A. Wilhelm and P. L. Grande, Unraveling energy loss processes of low energy heavy ions in 2D materials, Commun. Phys. **2**, 89 (2019).